Absorption and recurrence spectra of hydrogen in crossed electric and magnetic fields

S. Freund, R. Ubert, E. Flöthmann, and K. Welge*
Fakultät für Physik, Universität Bielefeld, D-33615 Bielefeld, Germany

D. M. Wang and J. B. Delos
Physics Department, College of William & Mary, Williamsburg, Virginia 23187-8795
(Received 21 July 2000; revised manuscript received 14 December 2001; published 2 May 2002)

The absorption spectrum of the hydrogen atom in crossed electric and magnetic fields was measured. The magnetic field was set at 6.002 T, and the electric field was fixed at several values from 750 to 1000 V/cm. The observations require several different theoretical methods for their interpretation: (1) The spectrum is ''unscaled,'' the recurrences are weak, and their periods vary with energy over the interval of the observations. This observation caused us to develop a chirped Fourier transform method to extract closed orbits from the measured spectra. (2) The absorption spectrum consists of quasidiscrete peaks superposed on a smoothly rising continuum. To interpret this observation, a theoretical model of the continuum absorption is created, and we get results consistent with the measurements. (3) The experiments distinguish between ''prompt'' and ''delayed'' electrons, corresponding to lifetimes of the excited hydrogen atoms that are, respectively, less than or greater than about 100 ns. (4) At high energies, the measured absorption spectrum contains some regular quasidiscrete states. We use an Einstein-Brillouin-Keller quantization method to identify these as states that lie close to the plane perpendicular to the magnetic field.

DOI: 10.1103/PhysRevA.65.053408 PACS number(s): 32.80.Rm, 03.65.Sq, 32.60.+i

I. INTRODUCTION

Studies of the behavior of atoms in crossed fields go back to the earliest days of quantum mechanics, and today there is renewed interest in this problem [1]. Recently, Tong and Chu [2] and Rao, Delande, and Taylor [3] carried out quantum calculations of high Rydberg states of hydrogen in crossed fields, and the latter interpreted the results using closed orbit theory. A few years ago, Raithel and Walther [4] reported a detailed experimental study of rubidium atoms in crossed fields. They observed many recurrences associated with closed orbits, examined long-lived vs short-lived states, and studied the ''threshold'' energy for ionization. They defined this ''threshold'' to be the energy at which half of the excited atoms have lifetime less than 20 μs. They found that it seems to follow classical scaling laws, and they proposed a mixed quantum-classical theory to explain its behavior.

Several other studies have also focused on the threshold for ionization. Uzer and Farrelly [5] examined the hydrogen atom in crossed fields theoretically, and they argued that the threshold should simply correspond to the saddle point, and thus should be independent of the magnetic field. Subsequently, Jaffé *et al.* [6] examined planar orbits of this system in more detail, and they interpreted ionization using a fractal tiling of the Poincaré plane. Presently these theories are not fully in accord with experiments; perhaps part of the problem is that they do not take account of the fact that electrons must begin close to the nucleus.

Other experiments and calculations focused on the lifetimes of excited states of atoms in fields. Koch and Mariani [7] measured the lifetimes of hydrogen atoms in electric fields. Lifetimes of excited states of organic molecules in an electric and in crossed electric and magnetic fields were studied in [8]. In these experiments, the excitation energy was fixed within a small range, and the time spectrum of escaping electrons was measured. The theoretical interpretation involved classical trajectory calculations including both elastic and inelastic scattering of the electron from the molecular ion core. Since the organic molecule constitutes a large, polar, and excitable core, we expect the behavior to be rather different from that in hydrogen.

Raković and Chu [9] discovered an integrable Hamiltonian system which is similar to the hydrogenic crossed-field system, but which possesses a full set of conservation laws. This is a stimulating discovery, but since the hydrogen atom undergoes chaotic ionization, it is unclear how helpful this integrable model can be.

In this paper, we report observations of the absorption spectrum of the hydrogen atom in crossed fields, and we report our theoretical interpretation of these results. In Sec. II, we discuss the crossed-fields system and its Hamiltonian, and we give an overview of our experimental results in Sec. III. Section IV is devoted to the interpretation of large-scale structure in the absorption spectrum. Our computational method, the chirped Fourier transform, is applied to extract short closed orbits. (Additional information about the chirped Fourier transform is given in the Appendixes.) Section V focuses on the interpretation of the observed continuum intensity and the ionization ''threshold.'' A theoretical model for calculating the continuum intensity is provided, and the results are presented. In Sec. VI, we report the observation of ''prompt'' vs ''delayed'' signals, but we leave the interpretation for future research. Long-lived regular quasidiscrete states are discussed in Sec. VII and a semiclassical theory [Einstein-Brillouin-Keller (EBK) quantization] is applied to interpret them. Section VIII gives a summary.

*Deceased.

II. THE SYSTEM AND ITS HAMILTONIAN

Assuming that the nucleus is fixed [10], the Hamiltonian function for an electron in a hydrogen atom with electric field along the $+x$ direction and magnetic field along the $+z$ direction is given by

$$\hat{H}=\frac{\hat{P}^2}{2}-\frac{1}{\hat{r}}+F\hat{x}+\frac{B}{2}\hat{L}_z+\frac{B^2}{8}(\hat{x}^2+\hat{y}^2). \tag{1}$$

With the following energy, electric field, coordinates, and momenta transformations: $f=FB^{-4/3}$, $\epsilon=EB^{-2/3}$, $r=\hat{r}B^{2/3}$, $P=\hat{P}B^{-1/3}$, the scaled Hamiltonian H is

$$H=\frac{P^2}{2}-\frac{1}{r}+fx+\frac{1}{2}L_z+\frac{1}{8}(x^2+y^2). \tag{2}$$

The equations of motion are singular at the origin, and this leads to difficulties in numerical computations. A method to eliminate the singularity was invented by Kustaanheimo and Stiefel (KS) [11]. This transformation expresses the close relationship between the three-dimensional hydrogen atom and a four-dimensional harmonic oscillator. In this transformation, configuration space is augmented from three coordinates to four coordinates, and phase space goes from six dimensions to eight dimensions (the eight-dimensional phase space is called KS space). The regularized Hamiltonian h is given by

$$h=4=p^2/2-4u^2\epsilon-8f(u_2u_1-u_4u_3)u^2+2(u_2p_3-u_3p_2)u^2+2(u_2^2+u_3^2)(u_1^2+u_4^2)u^2, \tag{3}$$

with $p^2=p_1^2+p_2^2+p_3^2+p_4^2$ and $u^2=u_1^2+u_2^2+u_3^2+u_4^2$. In this KS space, variables evolve in a fictitious time s, where s is defined by

$$\frac{dt}{ds}=4u^2=4r \tag{4}$$

and the equations of motion in KS space have canonical form.

III. EXPERIMENTAL RESULTS

In this section, we summarize the experimental procedure and give an overview of the results. The experiments are performed as in [12], with modifications in the inner apparatus (see Fig. 1).

Deuterium atoms in a beam collimated along the magnetic field axis (z axis) are excited at the center of the crossed fields by pulsed lasers perpendicular to the atomic beam. They are raised to high-energy states in two steps. In the first step from D($1s$) to D($2p$), we use an excimer-laser-pumped dye laser, frequency tripled to 121.6 nm, with $\Delta\nu_1\approx 1.8$ GHz. In the second step from D($2p$) to high-Rydberg states D*($n,m_l=0$) we use an excimer-laser-pumped dye laser, seeded by a single-frequency Ti:sapphire laser, frequency doubled to $\lambda_2\approx 365$ nm, with $\Delta\nu_2\approx 170$ MHz. Both lasers are linearly polarized along the magnetic-field

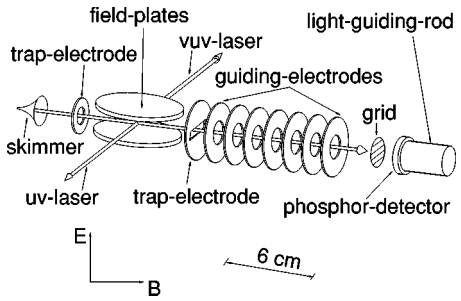

FIG. 1. Inner apparatus.

axis, which is called the z axis in this paper. To reduce any effects of blackbody radiation on the high-Rydberg states, the chamber is cooled to 77 K.

Electrons from atoms promptly ionized within the interaction region (short-lived states) are prevented from $\mathbf{E}\times\mathbf{B}$ drift by turning off the electric field about 100 ns after excitation. After the laser pulse, electrons are trapped for about 3.5 μs, and then they are guided by the ring electrodes to the detector. These electrons constitute what we call the ''prompt'' signal. They arrive in a short pulse which is artificially broadened by a RC circuit so that the area under the peak can be measured accurately. Meanwhile D* atoms in long-lived states are continuing to move at thermal velocity. About 30–180 μs after the laser pulse, the D* atoms arrive at the grid and are detected via electrons created by field ionization. These electrons constitute the ''delayed'' signal. The total absorption spectrum is the sum of the ''prompt'' signal and ''delayed'' signal.

It is important to understand the wide range of time scales involved in this experiment, because the interpretation of the measurements involves this range (see Fig. 2). Following we list the time scales and their connections with our observations.

(1) At the lowest energy in our observations, $E\sim -200$ cm^{-1}, the principal quantum number is about 24, and the Kepler orbit time is $(24)^3=1.4\times 10^4$ atomic units, or 3×10^{-13} s.

(2) At the magnetic field of 6 T, the cyclotron time is 2.46×10^5 atomic units, or 5.95×10^{-12} s. Recurrences corresponding to orbits having closure times of 0.3 to 1 cyclotron times are observed.

(3) Continuum absorption is also observed. We will show that this continuum is made up of states having lifetimes up to about 25 cyclotron times.

(4) The ''resolution time'' is $2\pi\hbar/\delta E$, where δE is the best resolution for this experiment (i.e., the smallest observable linewidth). The limiting resolution for this measurement is about 170 MHz, so the ''resolution time'' is 6×10^{-9} s.

(5) The effective laser pulse duration experienced by an atom is 12 ns. After this duration of the laser pulse, some of the electrons are in long-lived quasibound states, while others have gone to unstable states and quickly escape from the atom. The latter are the ''prompt'' electrons.

(6) The electric field is switched off about 100 ns after excitation. The promptly ionized electrons are trapped briefly, and then guided to the detector. In the process of switching off the electric field, the long-lived neutral atoms

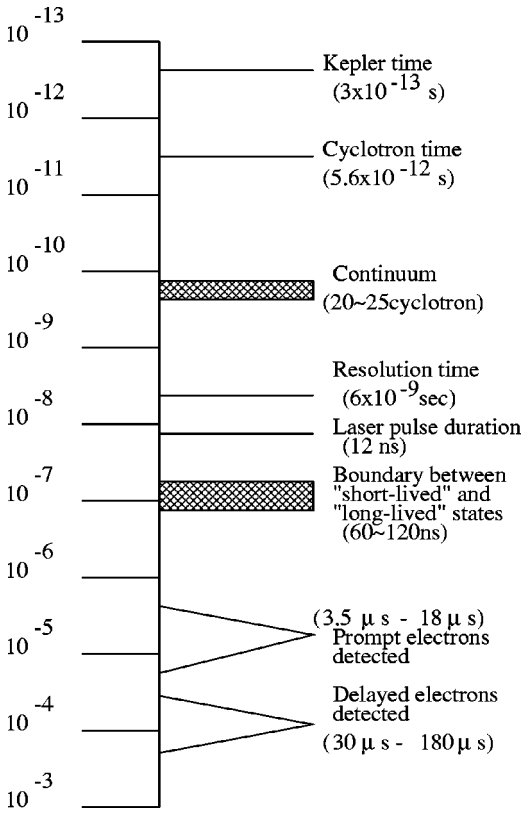

FIG. 2. Time scales involved in these measurements and their interpretation.

evolve, presumably adiabatically, from crossed-field states to pure-magnetic-field states. Long-lived neutral atoms were created at negative energies, and presumably remain at negative energies after the field is switched off, and therefore they are stable after 120 ns. We say, then, that the ''prompt'' electrons are those that are excited to states having lifetimes less than or of the order of 100 ns.

(7) After about 30–180 μs, the neutral atoms have traveled to a region of strong electric field where they are ionized and detected. These are the ''delayed'' electrons, which arise from crossed-field states having lifetimes greater than or of the order of 100 ns.

To test whether the overall detection efficiencies of long-lived and short-lived states are equal, we smooth the two data sets and sum them to see if the smoothed total absorption is reasonably independent of energy. The result suggests that we should multiply the delayed-electron signal by about 1.43 before comparing it with the prompt-electron signal. We have done this in all of our calculations.

Spectra are measured over a wide range (-195 to $+5$ cm^{-1}) at $B=6.002$ T and $F=1$ kV/cm, and then at higher resolution over a narrow range (-138 to -112 cm^{-1}) at $F=750$ to 1000 V/cm in steps of 50 V/cm.

An overview of the experimental observations is shown in Fig. 3 and Fig. 4. In Fig. 3, the saddle energy E_s is marked at -193 cm^{-1}. Most of the recorded spectrum is above this saddle energy. Just above this saddle energy, in the region marked *a*, all the electrons belong to the delayed signal, and the prompt signal is small. At higher energies near *b*, the

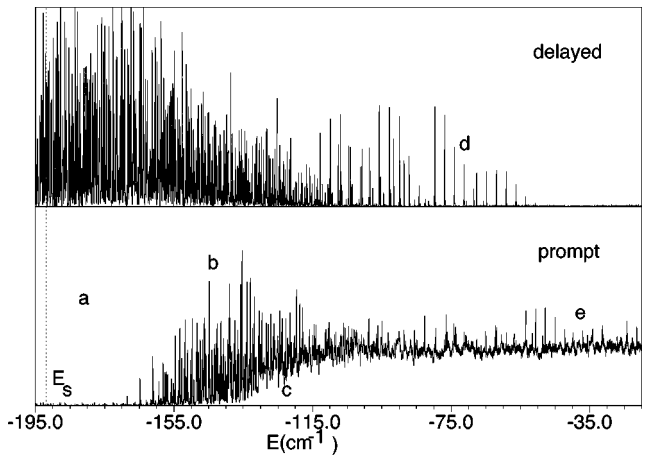

FIG. 3. The measured prompt and delayed absorption spectrum at $B=6.002$ T, $F=1000$ V/cm. The vertical axis represents measured relative absorption rate in arbitrary units vs energy. The dotted line marked E_s is the energy of the saddle point (-193 cm^{-1}).

prompt signal becomes significant. At still higher energies, near *c*, continuum absorption becomes evident. The spectrum is a set of narrow, quasidiscrete absorption lines superposed on this continuum. As the energy is raised further, more and more quasidiscrete states become broad and disappear into the continuum. Near *d* in the delayed signal, only a few quasidiscrete states survive and they seem to fall into a regular pattern. At energies near *e*, all the signal comes from prompt electrons, only a few narrow lines survive, and most of the absorption is continuum or broad lines. Figure 4 displays the measured total absorption spectrum superposed on the convoluted spectrum. Again we observe the clear distinction between saddle point and continuum threshold.

In the following sections, we provide theoretical interpretations of these measurements. In Sec. IV, we show recurrences corresponding to the short closed orbits having return times between 0.3 and 1 cyclotron times. The continuum that is plainly visible near mark *c* in Fig. 3 and in Fig. 4 is discussed in Sec. V. We show that this continuous absorption corresponds to that subset of the ''prompt'' electrons which arise from states having lifetimes less than 20–25 cyclotron times.

In Sec. VI, we give additional information about the measured ''prompt'' and ''delayed'' electron signals, and we show how this signal changes with changing electric field.

Finally, the regular long-lived states visible in Fig. 3 near *d* are discussed in Sec. VII. These states correspond to a regular family of quasiperiodic orbits that oscillate about a stable periodic orbit which lies in the plane perpendicular to the magnetic field.

IV. EXTRACTION OF RECURRENCES: THE CHIRPED FOURIER TRANSFORM

In Fig. 4, the wiggly line is a convolution of the measured absorption spectrum with a Gaussian function having standard deviation 2 cm^{-1}. The wavy structure in this line is correlated with short closed orbits. In order to extract the

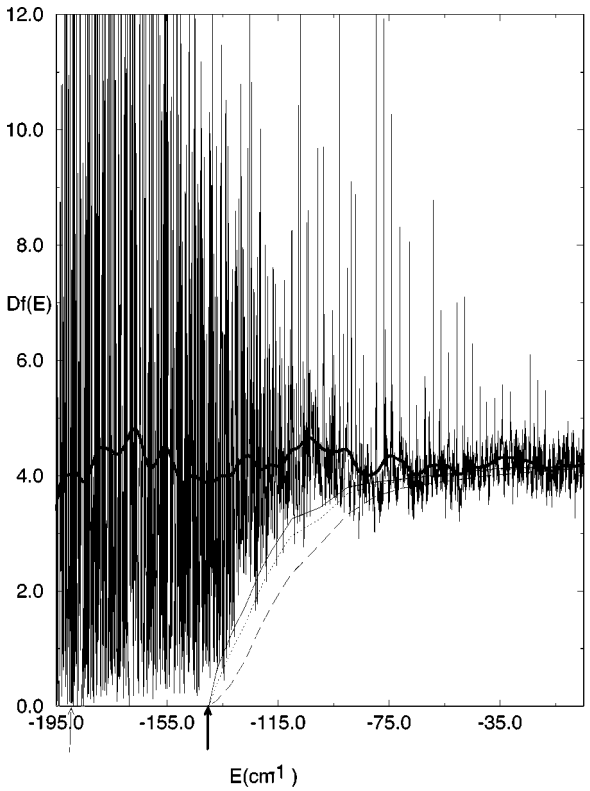

FIG. 4. The measured total absorption spectrum at $B=6.002$ T, $F=1000$ V/cm. The vertical axis represents oscillator-strength density in atomic units. The wiggly line is a convolution of the measurement with a Gaussian function having a standard deviation of 2 cm^{-1}; its fluctuations are correlated with closed orbits. The other curves are calculations based on a model for continuum absorption, discussed in Sec. V. From lowest to highest, they have $T_{crit}=15T_c$, $20T_c$, and $25T_c$ (respectively, long-dashed line, dotted line, and solid line). Light arrow: saddle energy E_s (-193 cm^{-1}). Heavy arrow: vicinity of fuzzy threshold for continuum absorption $[-140,-135]$ cm^{-1}. The experimental results have been normalized to theoretical values.

closed orbits from the measured absorption spectrum, we developed a computational technique called the chirped Fourier transform (CFT).

According to closed-orbit theory, the photoabsorption spectrum is given by a slowly varying background plus a sum of sinusoidal terms of the form

$$Df_{osc}(E)=\sum_j C_j(E)\sin[S_j(E)/\hbar-\pi\mu_j/2], \tag{5}$$

where j labels the closed orbits and their repetitions. μ_j is a Maslov index for the orbit (not important for this paper). $C_j(E)$ is the recurrence amplitude of each closed orbit. It contains information about the stability of the orbit, the initial and final angles of the orbit, and the matrix element of the dipole operator between the initial state and the zero-energy Coulomb wave. $S_j(E)$ is the classical action of the closed orbit, which satisfies

$$\partial S_j(E)/\partial E=T_j(E), \tag{6}$$

where $T_j(E)$ is the return time of the orbit. If the return time is nearly independent of E over the range of the measurement, then Eq. (5) gives a nearly sinusoidal oscillation having wavelength (on the energy axis) equal to $2\pi\hbar/T_j$, and the Fourier transform will show a peak at $T=T_j$. This method has been successfully applied to several measurements [13,14]. However, our measurements in crossed fields are different from those of [13,14] in the following two aspects.

(a) The papers [13,14] consider cylindrically symmetric systems. According to [15], the recurrences in a noncylindrically symmetric system are weaker than those found in cylindrically symmetric systems. In a cylindrically symmetric system, each "closed orbit" is actually a cylindrical family of closed orbits and each family may be identified by the initial polar angle θ of the outgoing electron which returns regardless of its initial azimuthal angle ϕ. In the crossed-field system, the electron returns to the atom only if both the initial polar and azimuthal angles of the outgoing electron are correct. Therefore the recurrence amplitudes C_j in the crossed-field system are smaller than those in cylindrically symmetric systems. Using notation defined in Ref. [13], the formula for C_j is [16]

$$C_j(E)=(E-E_i)2^{9/2}\pi r_b^{-1/2}A_j(q_{ret}) \times y^*(\theta^j_{ret},\phi^j_{ret})y(\theta^j_{out},\phi^j_{out}). \tag{7}$$

Here

$$y(\theta,\phi)=\sum_{l_1m_1} I(n,l,l_1)b_{l_1,m_1}Y_{l_1m_1}(\theta,\phi) \tag{8}$$

is the angular distribution of outgoing electrons evaluated at the outgoing and returning angles of the orbit; it involves radial parts of dipole integrals $I(n,l,l_1)$ between the initial state and a zero-energy Coulomb wave, and Clebsch-Gordan coefficients b_{l_1,m_1}. $A_j(q_{ret})$ is the square root of the classical density,

$$A_j(q_{ret})=\sqrt{J(t=0)/J(t_{ret})}, \tag{9}$$

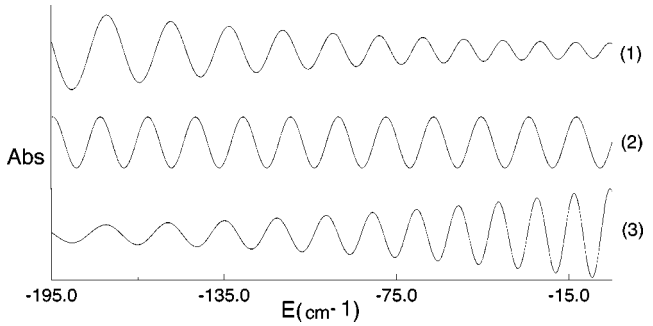

FIG. 5. (1) Theoretical absorption (i.e., oscillator-strength-density in arbitrary units) vs energy associated with the shortest trajectory; (2) $\sin(TE)$; (3) $\exp[\gamma(E-E_0)]\sin[T(E-E_0)+\alpha(E-E_0)^2+\beta(E-E_0)^3]$.

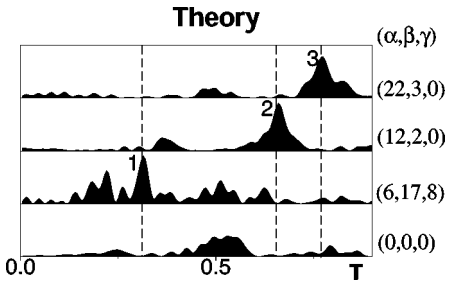

FIG. 6. Theoretical recurrence spectra for $B=6$ T, $F=1$ kV/cm using the chirped Fourier transform, at appropriate values of α,β,γ. Time is measured in units of the cyclotron time at 6.002 T (5.95×10^{-12} s). The dashed lines represent the return times of the three shortest closed orbits shown in Fig. 8. α,β,γ are the coefficients in the chirped Fourier transform and they are in units of $1/\mathrm{cm}^{-1}$, cyclotron times/cm^{-1}, cyclotron times/cm^{-2}. α,β,γ should be multiplied by $10^{-4},10^{-6},10^{-3}$, respectively; thus, for example, the calculated and observed value of α_1 is 6×10^{-4}. (Units of the vertical axis are undefined.) In the ordinary Fourier transform (lowest curve), no signal of closed orbits is visible, but in the chirped transform, each closed orbit gives a clear peak. See also Fig. 15 below.

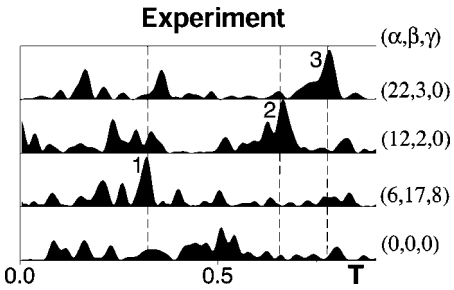

FIG. 7. Chirped Fourier transforms of the experimental spectrum, as in Fig. 6.

where J is the Jacobian $\partial(x,y,z)/\partial(t,\theta_{out},\phi_{out})$, which is associated with the classical density. All quantities in these equations are defined fully in Ref. [13].

(b) Our measurements are done with fixed field strengths and varying photon energy, whereas the measurements in [13,14,4] were done by the scaled-variables method. In the present case, the return time of each orbit varies with energy, so each corresponding peak in the Fourier transform is low and broad. More precisely, many cannot be seen at all. Therefore we need a different computational method to extract the recurrences from this spectrum.

In Fig. 5 curve 1, we show the contribution of the shortest closed orbit to the absorption spectrum, as calculated from Eq. (5). As a function of energy, $C_1(E)$ gradually decreases while $T_1(E)$ increases, and we get a chirped sine wave. If we perform an ordinary Fourier transform, we multiply a chirped wave by a perfect sine wave (see curve 2 in Fig. 5), and then integrate. Over the range of integration, waves 1 and 2 keep drifting in and out of phase, so we may get only a low and broad peak in the recurrence spectrum. However, if we multiply the chirped wave by another chirped wave (see curve 3 in Fig. 5) with the same change in phase and the opposite change in amplitude compared to the original chirped wave, and then integrate, we get a sharp peak in the recurrence spectrum. This is the basic idea of the chirped Fourier transform.

Let us represent the return time of each closed orbit as a Taylor expansion in energy,

$$T_j(E)=T_j(E_0)+2\alpha_j(E-E_0)+3\beta_j(E-E_0)^2, \quad (10)$$

and approximate the amplitude $C_j(E)$ by an exponential function

$$C_j(E)=C_j(E_0)\exp[-\gamma_j(E-E_0)/\hbar]. \quad (11)$$

A corresponding chirped Fourier transform is defined as [17]

$$\tilde{D}f(T;\alpha,\beta;\gamma)=\int_{E_1}^{E_2}Df(E)e^{-i[T(E-E_0)+\alpha(E-E_0)^2+\beta(E-E_0)^3]/\hbar+\gamma(E-E_0)/\hbar}dE, \quad (12)$$

where E_0 is some point in the middle of the observed range, and α,β,γ are three independent parameters.

Figures 6 and 7 display the chirped Fourier transform of the energy spectrum as a function of T with various selected values of α, β, and γ. The family of curves marked ''experiment'' are the CFTs of the total absorption spectrum shown in Fig. 4. The family of curves marked ''theory'' were obtained by calculating the action $S_j(E)$ and the recurrence amplitude $C_j(E)$ for the five shortest orbits, and then taking the CFTs of Eq. (5). The dashed lines indicate the return times of the three shortest closed orbits illustrated in Fig. 8. In each figure, the lowest curve, $\alpha=0,\beta=0,\gamma=0$, is the ordinary Fourier transform. We see hardly any relationship between the results and the known closed orbits. The other curves have α,β,γ as indicated. We arrived at these values by both experimental and theoretical methods. (1) With no knowledge of $T_j,\alpha_j,\beta_j,\gamma_j$, one can search in the parameter space to make a peak in the CFT as a function of T as high and narrow as possible. In this case, we had already computed theoretical values of T_j, so we knew where to look for peaks. We gradually increased α to sharpen a peak, then turned on β, then (if necessary) turned on γ. (2) By computing properties of classical orbits, we found theoretical values of $T_j,\alpha_j,\beta_j,\gamma_j$. These different approaches gave consistent results.

The experimental and theoretical results agree with each other adequately. The experiment shows many additional, ''false'' peaks, and in the Appendixes we show how the CFT

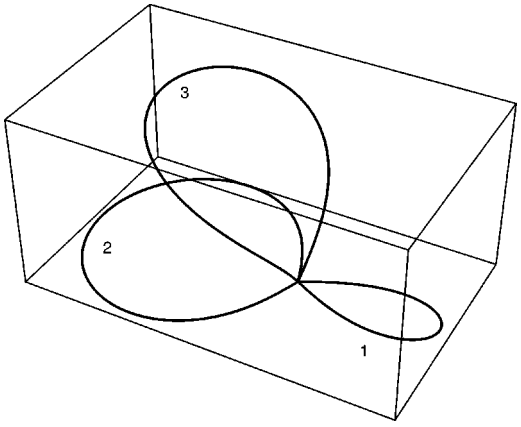

FIG. 8. Three shortest closed orbits identified in Fig. 7 for $B=6$ T, $F=1$ kV/cm.

can give significant ''aliasing.'' Nevertheless, the largest peaks have the correct values of (T,α,β,γ). This consistency confirms the validity and applicability of the appropriate closed-orbit formula for this system. It also establishes that the CFT is a useful tool for extracting recurrences. We notice that the observations give measured values of α,β within uncertainties less than $\pm 1\%, \pm 5\%$. In many applications of closed-orbit or periodic-orbit theory, scaled-variable spectroscopy might be difficult or impossible to use. In such cases, the chirped Fourier transform gives a way to extract classical information from a quantum spectrum directly [18]. In Appendix A, we give additional theory of the CFT and another application is shown in Appendix B.

V. THE OBSERVED AND CALCULATED CONTINUUM INTENSITY AND THRESHOLD FOR CHAOTIC IONIZATION

If we examine either the prompt signal in Fig. 3 or the total signal in Fig. 4, it is reasonable to say that at low energies (from *a* to *b*), we have only narrow quasidiscrete absorption lines, at intermediate energies (around *c*), we have quasidiscrete lines superposed on a continuum, and at high energies, the quasidiscrete lines have become sparse. The threshold of continuum absorption is not sharp, but we may reasonably say that substantial continuum absorption begins near the heavy arrow in Fig. 4, around -140 to -135 cm^{-1}. This is well above the saddle point, which is near -195 cm^{-1}. In this section, we provide a theoretical model to compute the continuum intensity and interpret this fuzzy threshold.

First let us review the behavior of a hydrogen atom in a pure electric field ($B=0$). In that case [19], the potential energy has a saddle point with saddle energy $E_s=-2F^{1/2}$. For energies between E_s and zero, the classical electron has both bound and free states. There is a sharp boundary between these bound and free states, defined by a critical angle of ejection from the atom, $\theta_c=\arccos(1-E^2/2F)$. The sector with ejection angle from θ_c to π is called the escape sector and the sector with ejection angle from 0 to θ_c is called the bound sector. Electrons ejected in the bound sector are bound forever, while electrons ejected in the escape sector pass over the saddle and then escape. As the energy increases from E_s to zero, this critical angle moves from the downhill to the uphill direction until no stable bound motion is left. This classical behavior is manifested in the absorption spectrum. Above the saddle (and below $E=0$), the absorption spectrum exhibits narrow quasidiscrete states superposed on a smooth background. The continuous background arises from the electrons that leave the atom in the escape sector, while the quasidiscrete states are correlated with electrons that leave in the bound sector. The observed threshold of the continuum is precisely the saddle point energy, and absorption to the continuum is proportional to the current of electrons leaving the atom in the escape sector. As the energy is raised from the saddle energy to $E=0$, and the critical angle moves from π (downhill) to 0 (uphill), absorption into the continuum increases, and each quasidiscrete state becomes broad until it becomes part of the continuum.

When the magnetic field is added, the boundary between bound and free motions becomes fuzzy. We have calculated the escape time of an electron as a function of its polar and azimuthal angles from the downhill direction [26,27]. Complex structure is observed, and when calculations are carried out to higher resolution, structure within structure is found. It is reasonable to believe that there is some sort of fractal boundary between bound and free motions. Indeed, Jaffé *et al.* examined planar orbits of this system, and proposed a fractal tiling of the escape region of the Poincaré plane [6].

The intensity of continuum absorption should be proportional to the flux of escaping electrons, which is defined as [19]

$$Df(E)=4(E-E_i)\int_{escape}|y(\theta,\phi)|^2\sin\theta d\theta d\phi, \quad (13)$$

where $|y(\theta,\phi)|^2$ is the angular distribution of outgoing waves, and the integral is carried out over the escape sector. In the pure-electric-field case, the escape sector has a sharp boundary, and there is no ambiguity about the meaning of Eq. (13). However, in crossed fields, the escape sector has no exact definition. We define the escape sector so that it includes electrons that escape in times less than some chosen T_{crit}.

Specifically we calculate the integral (13) in the following way. We sample θ and ϕ uniformly in solid angle (equal number of trajectories in equal increments of solid angle), with $\Delta\theta\approx 1°$ and $\Delta\phi$ proportional to $\Delta\theta/\sin\theta$. At each (θ_i,ϕ_i), we launch a trajectory and find the time required for escape. (We choose the escape condition $|x|>2|x_s|$ where x_s is the position of the saddle point.) If the escape time is less than T_{crit}, we include the increment $|y(\theta_i,\phi_i)|^2\sin\theta_i\Delta\theta_i\Delta\phi_i$ in the integral; otherwise we do not.

To get a preliminary estimate of T_{crit}, we examined the absorption spectrum at high resolution, and asked what are the broadest structures that would reasonably be called quasidiscrete states. We found such structures with widths about 0.25 cm^{-1}, which correspond to lifetimes $T=2\pi\hbar/\Delta E$ of about 22 cyclotron times. Therefore we tried values of T_{crit} between 15 and 30 cyclotron times.

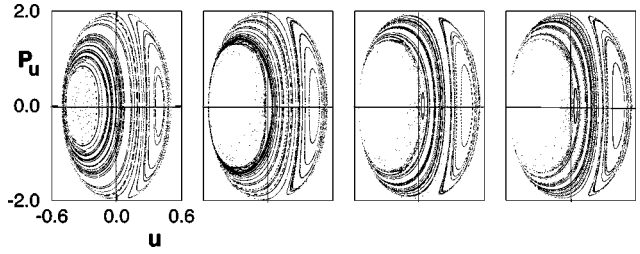

FIG. 9. A collection of surfaces of section at $B=6$ T, $F=1000$ V/cm with varying energy. From left to right, $E=-193$ cm^{-1} (saddle energy), -150 cm^{-1}, -140 cm^{-1}, and -135 cm^{-1}. $[-140,-135]$ cm^{-1} is the vicinity of the fuzzy threshold for ionization.

Finally, to compare with the measured spectrum, we normalize the measured spectrum so that its average at high energies is equal to

$$Df_0 \equiv 4(E-E_i)\int_0^{2\pi}\int_0^{\pi}|y(\theta,\phi)|^2 \sin\theta d\theta d\phi.$$

Figure 4 shows our normalized calculated continuum absorption for three selected values of T_{crit}, together with the measured total absorption spectrum. We find that continuum-absorption in this system can be interpreted as the flux of electrons that escape within 20–25 cyclotron times.

Next we consider the fuzzy boundary of the continuum. In Fig. 4, we put a heavy arrow at $E\approx(-140,-135)$ cm^{-1} to indicate a reasonable location of this fuzzy boundary, which is substantially higher than the saddle point energy (-193 cm^{-1}). Therefore we observe that the magnetic field stabilizes the classical motion. This is consistent with observations in [4] but inconsistent with the theoretical arguments in [5].

This discrepancy is not hard to resolve. Uzer and Farrelly are correct in their observation that at all energies above the saddle point there is a region of phase space corresponding to chaotic ionization. However, in these spectroscopic experiments, all electrons begin their orbits close to the nucleus. Only at an energy significantly higher than the saddle energy can these electrons escape from the atom on classically allowed orbits.

To see this, let us examine motions in the plane perpendicular to the magnetic field. Figure 9 shows some surface of section calculations. In our calculation, we use semiparabolic coordinates in the plane perpendicular to B, that is, $u=(r+x)^{1/2}, v=(r-x)^{1/2}$. Then the u axis coincides with the positive x axis (uphill) and the v axis coincides with the negative x axis (downhill). In the surface of section, we plot (p_u,u) at $v=0, p_v>0$. Therefore, the p_u axis in this figure corresponds to the location of the nucleus (the origin of coordinates), and $p_u=0$ means that all the energy is ''in the v direction,'' i.e., downhill.

From Fig. 9, we observe a regular region on the right, where electrons stay bound forever, and a chaotic zone on the left, where electrons remain for a while before escaping, as well as a ''white hole'' on the left, where electrons escape rapidly. We find that the chaotic and escape zones increase rapidly in size as the energy is increased above the saddle energy. However, electrons that start from the nucleus ($u=0$) remain on regular, bound orbits until the chaotic zone touches the momentum axis. When we continue to increase the energy, an increasing portion of the momentum axis lies within the chaotic and escape zones, which means that electrons which start from the origin in a range of directions escape. Comparison between these calculated surfaces of section and the measurements indicate that the observed fuzzy boundary of the continuum is the energy at which the chaotic zone first touches the momentum axis. At this energy, trajectories launched at the origin may escape from the atom within a short time. From Fig. 9, we observe that this fuzzy boundary for chaotic ionization of electrons that begin at the nucleus is around -140 cm^{-1}.

Measurements and calculations at other electric fields also support this interpretation. The observed fuzzy threshold of the continuum corresponds to the calculated boundary for chaotic ionization of electrons ejected from the origin, and this observed fuzzy boundary is higher than the saddle energy.

VI. "PROMPT" VS "DELAYED" ELECTRONS

The measurements also give some information about the lifetimes of long-lived excited states. Such information can give clues about the mechanism of ionization of these states, or at least provide a check of theory.

In the introduction, we cited other studies of lifetimes of atoms in fields. Only [7] examines hydrogen, and no magnetic field is present in that experiment. In [8], electric and magnetic fields are fixed, energy is fixed within a small range, and the time spectrum of electrons escaping from an organic molecule is measured. The experiment most similar to ours is that done by Raithel and Walther [4]; at various energies and field strengths, they distinguish ''prompt'' and ''delayed'' electrons escaping from Rb. In their apparatus, the boundary between prompt electrons (short-lived atomic states) and delayed electrons (long-lived atomic states) is about 20 μs.

In our experiments on hydrogen, the prompt signals correspond to excited atoms with lifetime less than 120 ns and the delayed signals correspond to excited atoms with lifetime greater than 120 ns. (Note that there is no relation between this boundary and the value of $T_{crit}\simeq 130$ ps associated with continuum absorption.) Figure 3 shows the measured prompt and delayed signals at $B=6.002$ T and $F=1000$ V/cm. In this section, we show how the prompt and delayed signals change as the electric field changes.

Figure 10 displays the convoluted prompt and delayed signals. The prompt signal increases with energy and the delayed signal decreases with energy. The crossing of the fast and slow signals moves toward lower energy with increasing electric field. Oscillatory structures mostly are in phase in both prompt and delayed signals, and we believe them to be associated with closed orbits. Currently, there are no theoretical calculations to interpret these results, and we leave this as an open problem.

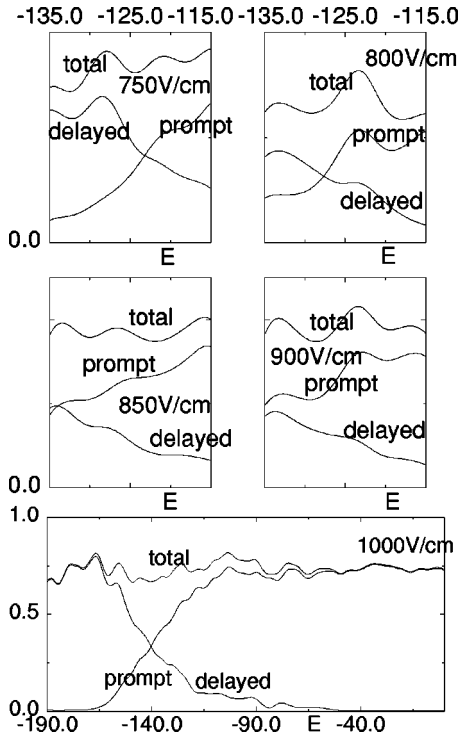

FIG. 10. Measured relative convoluted prompt and delayed absorption spectra at $B=6.002$ T and various electric fields labeled in the graphs. The energy is in cm^{-1}.

VII. LONG-LIVED REGULAR QUASIDISCRETE STATES

In Fig. 3 near *d*, we observe the presence of a regular sequence of narrow absorption lines in the ''delayed'' spectrum. In this section, we show that these lines correspond to a regular family of quasiperiodic orbits. For the crossed-field system, there are two elementary periodic orbits (S_+, S_-) which were well studied by Flöthmann and Welge [20]. These two lie in the plane perpendicular to the magnetic field, and S_+ goes around in a right hand sense relative to $\vec{\boldsymbol{B}}$. On this orbit, the Coulomb force and the Lorentz force both point inward. This orbit is stable and quasielliptical in the energy range we study. Quasiperiodic orbits oscillate about S_+, and these orbits occupy a sufficient volume of phase space to support quantum states.

In EBK theory, each quantum state corresponds to a torus having classical actions restricted to certain integer or half-integer values. The main challenge involved in EBK quantization is the determination of the action variables, which are defined as integrations around independent loops on the torus. Hence we need to determine the independent loops in our system. For systems with one or two degrees of freedom, caustics [21] or Poincaré surfaces of section [22] provide convenient methods to determine the independent loops. However, for systems with more than two degrees of freedom, these methods become difficult [23].

Another method, based on the Fourier transform, was developed by Martens and Ezra [24,25]. In this section, we adapt the same idea to obtain the independent loops and the action variables. The key point of this method is calculation of the angle-parametrized torus from a numerically integrated regular trajectory by Fourier transformation.

A. The theory of the Fourier transform method

The main theme of the Fourier transform method can be summarized in three points.

(1) The time dependent Fourier series of the variables of a regular trajectory. By integrating equations of motion, we obtain a numerical representation of $[u_i(s), p_i(s), t(s)]$ for a regular trajectory [11]. By putting $[u_i, p_i]$ into the KS transformation, we can convert the KS variables $[u_i(s), p_i(s), t(s)]$ to the Cartesian variables $[q_i(s), P_i(s)]$ or $[q_i(t), P_i(t)]$. According to [24], regular motion is quasiperiodic with three independent fundamental frequencies $\boldsymbol{\omega} = (\omega_1, \omega_2, \omega_3)$, so the variables can be expressed as [24]

$$\mathbf{q}(t) = \sum_{\mathbf{k}} \mathbf{q}_{\mathbf{k}} \exp[i\mathbf{k}\cdot(\hat{\boldsymbol{\omega}}t + \boldsymbol{\beta})], \tag{14}$$

$$\mathbf{P}(t) = \sum_{\mathbf{k}} \mathbf{P}_{\mathbf{k}} \exp[i\mathbf{k}\cdot(\hat{\boldsymbol{\omega}}t + \boldsymbol{\beta})] \tag{15}$$

or

$$\mathbf{q}(s) = \sum_{\mathbf{k}} \mathbf{q}_{\mathbf{k}} \exp[i\mathbf{k}\cdot(\boldsymbol{\omega}s + \boldsymbol{\beta})], \tag{16}$$

$$\mathbf{P}(s) = \sum_{\mathbf{k}} \mathbf{P}_{\mathbf{k}} \exp[i\mathbf{k}\cdot(\boldsymbol{\omega}s + \boldsymbol{\beta})] \tag{17}$$

where $\mathbf{k} = (k_1, k_2, k_3)$ is a vector of integers, and $\boldsymbol{\beta} = (\beta_1, \beta_2, \beta_3)$ are the initial phases.

In our system, coordinates expressed as functions of *s* vary more smoothly than those expressed as functions of *t*; therefore the Fourier series in *s* are simpler and have better convergence than those in *t* [see Figs. 11(b) and 11(d)]. Therefore, we Fourier-transform the numerical data of the variables in *s* to determine the fundamental frequencies, the amplitude of each oscillatory term, and the initial phases.

One more aspect of the numerical procedure is interesting. We carry out numerical integration of trajectories in eight-dimensional KS space. In this space, the tori are four-dimensional, and there are four independent fundamental frequencies. (In KS space, the periodic orbit S_+ is a two-torus.) However, when we evaluate the Cartesian variables, there are only three independent frequencies. We conclude that the nonlinear KS transformation $(\mathbf{u}, \mathbf{p}) \rightarrow (\mathbf{q}, \mathbf{P})$ eliminates one of the four frequencies. Further details are presented in [26].

(2) The angle-parametrized torus from a regular trajectory. Regular motion admits action-angle variables $(\boldsymbol{\theta}, \boldsymbol{I})$ with properties that the actions $\boldsymbol{I} = (I_1, I_2, I_3)$ are constant and the angles $\boldsymbol{\theta} = (\theta_1, \theta_2, \theta_3)$ evolve linearly in time:

$$\boldsymbol{\theta}(s) = \boldsymbol{\omega}s + \boldsymbol{\beta}. \tag{18}$$

Then the Fourier series of the variables can be interpreted as the transformation equations from $(\boldsymbol{\theta}, \boldsymbol{I})$ to $(\mathbf{q}, \mathbf{P})$ with fixed actions:

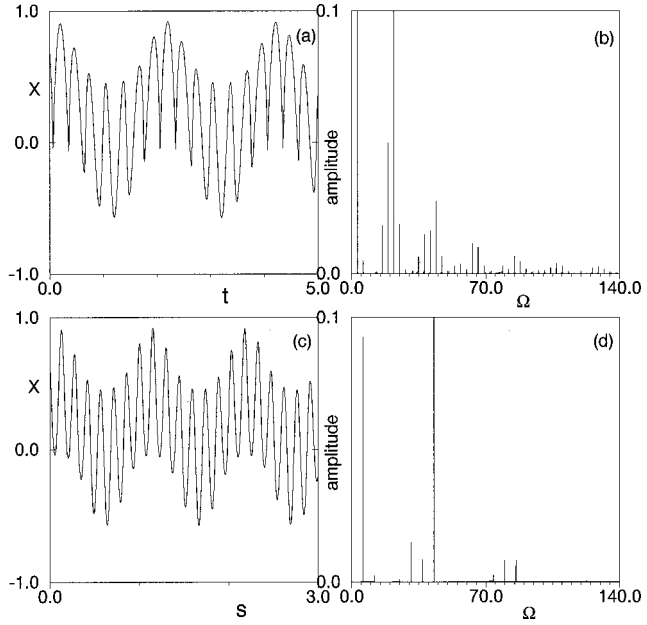

FIG. 11. Behavior of variables for the trajectory drawn in Fig. 12 below. (a),(b) $x(t)$ and its Fourier transform. (c),(d) $x(s)$ and its Fourier transform. $x(t)$ has rather sharp cusps when the electron comes close to the nucleus, so its Fourier transform has many high harmonics. $x(s)$ is smoother, so its Fourier transform has fewer harmonics.

$$\mathbf{q}(\boldsymbol{\theta},\boldsymbol{I})=\sum_{\mathbf{k}}\ \mathbf{q}_{\mathbf{k}}e^{i\mathbf{k}\cdot\boldsymbol{\theta}}, \tag{19}$$

$$\mathbf{P}(\boldsymbol{\theta},\boldsymbol{I})=\sum_{\mathbf{k}}\ \mathbf{P}_{\mathbf{k}}e^{i\mathbf{k}\cdot\boldsymbol{\theta}}. \tag{20}$$

This is the angle-parametrized torus.

Since $\mathbf{q}$ and $\mathbf{P}$ must be real, then $\mathbf{q}_{\mathbf{k}}$ and $\mathbf{P}_{\mathbf{k}}$ must satisfy $\mathbf{q}_{\mathbf{k}}^{*}=\mathbf{q}_{-\mathbf{k}}$ and $\mathbf{P}_{\mathbf{k}}^{*}=\mathbf{P}_{-\mathbf{k}}$. Let $\mathbf{q}_{\mathbf{k}}=|\mathbf{q}_{\mathbf{k}}|e^{i\phi_{\mathbf{q}_{\mathbf{k}}}}$ and $\mathbf{P}_{\mathbf{k}}=|\mathbf{P}_{\mathbf{k}}|e^{i\phi_{\mathbf{P}_{\mathbf{k}}}}$. We rewrite the angle-parametrized torus equation as

$$\mathbf{q}(\theta_1,\theta_2,\theta_3)=\mathbf{q}_{000}+2{\sum_{\mathbf{k}}}'\ |\mathbf{q}_{\mathbf{k}}|\cos(\mathbf{k}\cdot\boldsymbol{\theta}+\phi_{\mathbf{q}_{\mathbf{k}}}), \tag{21}$$

$$\mathbf{P}(\theta_1,\theta_2,\theta_3)=\mathbf{P}_{000}+2{\sum_{\mathbf{k}}}'\ |\mathbf{P}_{\mathbf{k}}|\cos(\mathbf{k}\cdot\boldsymbol{\theta}+\phi_{\mathbf{p}_{\mathbf{k}}}), \tag{22}$$

where the primed summation includes the terms with $\mathbf{k}\cdot\boldsymbol{\omega}>0$ only.

(3) Three independent loops and the actions along the loops. Three independent loops can be defined as loops with one angle variable varying from 0 to 2π and the other two angles fixed. The independent loops C_i in Fig. 12 are the loops with θ_i varying from 0 to 2π and θ_j,θ_k equal to zero:

$$\mathbf{q}(\theta_i)=\mathbf{q}_{000}+2{\sum_{\mathbf{k}}}'|\mathbf{q}_{\mathbf{k}}|\cos(k_i\theta_i+\phi_{\mathbf{q}_{\mathbf{k}}}), \tag{23}$$

$$\mathbf{P}(\theta_i)=\mathbf{P}_{000}+2{\sum_{\mathbf{k}}}'\ |\mathbf{P}_{\mathbf{k}}|\cos(k_i\theta_i+\phi_{\mathbf{p}_{\mathbf{k}}}). \tag{24}$$

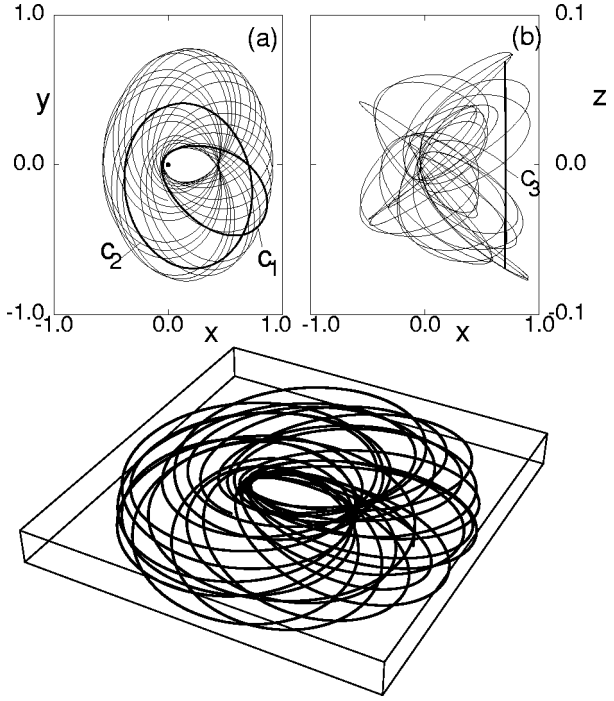

FIG. 12. The torus explored by the trajectory launched at $E=-110\ \mathrm{cm}^{-1}$ or $\epsilon=-0.5779$, $\theta=87°$, and $\phi=140°$, and the three loops C_i with $i=(1,2,3)$ used to calculate the actions. In (a) and (b) we show the loops and the trajectory in two-dimensional spaces xy and xz, and below we show the trajectory in a three-dimensional graph. (Note the small range of z motion.) The first loop C_1 touches two caustics, and includes one loop of angular motion and one loop of radial motion; the second loop C_2 is a loop of angular motion and it touches no caustics; the third loop is one loop of z motion, touching two caustics.

Then the actions along the loops are

$$I_i=(1/2\pi)\oint_{c_i}\mathbf{P}\cdot d\mathbf{q}=(1/2\pi)\oint_{c_i}\mathbf{P}\cdot\frac{d\mathbf{q}}{d\theta_i}d\theta_i. \tag{25}$$

Substituting the loop functions of $\mathbf{q}(\theta_i)$ and $\mathbf{P}(\theta_i)$ into Eq. (25) and performing the integration give us

$$I_i=2{\sum_{\mathbf{k}}}'\ k_i|\mathbf{q}_{\mathbf{k}}||\mathbf{P}_{\mathbf{k}}|\cos(\phi_{\mathbf{q}_{\mathbf{k}}}-\phi_{\mathbf{p}_{\mathbf{k}}}). \tag{26}$$

The actions depend on $\mathbf{k}$ not only through the amplitudes $\mathbf{q}_{\mathbf{k}}$ and $\mathbf{P}_{\mathbf{k}}$ but also through the phases of $\mathbf{q}_{\mathbf{k}}$ and $\mathbf{P}_{\mathbf{k}}$. This is different from Refs. [24,25], where the actions depend on $\mathbf{k}$ only through the amplitudes of $\mathbf{q}_{\mathbf{k}}$. The determination of phases requires high precision in the determination of the fundamental frequencies. We develop a method to achieve precision 10^{-7} in the determination of the frequencies. This method is discussed in [26]. Examining Fig. 12, we rename the loops (C_1,C_2,C_3) as $(C_{\rho+\phi},C_{\phi},C_z)$, and the corresponding action variables as $(I_{\rho+\phi},I_{\phi},I_z)$.

B. The semiclassical energy spectrum

We are interested only in the energy eigenvalues, so we calculate the actions $(I_{\rho+\phi},I_{\phi},I_z)$ of trajectories with vary-

ing initial conditions at varying energies and then fit the data set $(I_{\rho+\phi}, I_\phi, I_z, E)$ to a smooth function,

$$E = a_0 + a_1 I_{\rho+\phi} + a_2 I_\phi + a_3 I_z + a_4 I_{\rho+\phi}^2 + a_5 I_\phi^2 + a_6 I_z^2 a_7 I_{\rho+\phi} I_\phi + a_8 I_{\rho+\phi} I_z + a_9 I_\phi I_z . \quad (27)$$

Then we input the quantized actions to find the corresponding energy eigenvalues [22]. Numerical experiment shows that the fit function of Eq. (27) is accurate to about 10^{-2} cm^{-1}. Further details are presented in [26].

According to EBK quantization theory, the quantization conditions for $I_{\rho+\phi}, I_\phi, I_z$ are

$$I_{\rho+\phi} = n_{\rho+\phi} + 1/2,$$

$$I_\phi = n_\phi ,$$

$$I_z = n_z + 1/2,$$

where the half integer results from the fact that the loops $C_{\rho+\phi}$ and C_z each touch caustics twice. We also define a total action I as

$$I = I_{\rho+\phi} + I_z ,$$

so the quantization condition for I is

$$I = n = n_{\rho+\phi} + n_z + 1.$$

We call n the principal quantum number. Since there is a one-to-one correspondence between the eigentori (whose actions satisfy the quantization condition) and the quantum states, we can use $(n_{\rho+\phi}, n_\phi, n_z)$ or (n, n_ϕ, n_z) to label the states. Here we use the latter.

Our calculation shows that the states we identify all have n_z equal to zero: they have only ''zero-point'' motion out of plane. Therefore we use only (n, n_ϕ) to label the states. In Table I, we list the semiclassical energy eigenvalues with the quantum numbers. We also list the experimental values and the values obtained by a quantum mechanical method [27] for comparison. The accuracy of the experiment is 0.007 cm^{-1}. We mark the identified states on the measured absorption spectrum graph (see Fig. 13). The states in the energy range near d in Fig. 3 fall into several sequences. Each sequence is distinguished by the principal quantum number n, and the members of a sequence are distinguished by the azimuthal quantum number n_ϕ. Hence we have proved that the regular quasidiscrete states in the absorption spectrum correspond to regular tori which stay close to the xy plane and oscillate around the stable periodic orbit S_+.

TABLE I. List of the energy eigenvalues E_{expt}, $E_{quantum}$, and E_{semi}.

n	n_ϕ	E_{expt} (cm^{-1})	$E_{quantum}$ (cm^{-1})	E_{EBK} (cm^{-1})
26	9	−118.66132		−118.62790
26	10	−115.71537	−115.73	−115.71750
26	11	−112.77931	−112.79	−112.78747
26	12	−109.86435	−109.86	−109.83005
26	13	−106.96499	−106.97	−106.96124
26	14	−104.11635	−104.10	−104.09301
26	15	−101.23860	−101.23	−101.22536
26	16	−98.27655	−98.30	−98.25884
26	17	−95.37632	−95.39	−95.34356
26	18	−92.48411	−92.51	−92.54291
26	19	−89.92901	−89.94	−89.95688
27	4	−119.83373		−119.82059
27	5	−116.74612	−116.80	−116.75103
27	6	−113.66907	−113.71	−113.69182
27	7	−110.61467	−110.64	−110.60441
27	8	−107.57874	−107.61	−107.58828
27	9	−104.57000	−104.59	−104.57163
27	10	−101.59217	−101.25	−101.50445
27	11	−98.61679	−98.65	−98.61998
27	12	−95.70321	−95.72	−95.65637
27	13	−92.80433	−92.82	−92.80165
27	14	−89.65549	−89.65	−89.71642
27	15	−87.07754	−87.09	−87.07008
27	16	−84.26893	−84.26	−84.27282
27	17	−81.47313	−81.46	−81.47466

VIII. CONCLUSION

In this paper, we have presented experimental measurements of the absorption spectrum of a hydrogen atom in crossed electric and magnetic fields, and we have provided an interpretation of the measured data.

(1) We developed a computational method, the chirped Fourier transform, to extract closed orbits from an unscaled spectrum. Although scaled-variable spectroscopy is a superior method when it is available, the CFT is an effective way to extract closed orbits in systems for which scaled-variable spectra are impossible or unavailable.

(2) We built a theoretical model to calculate continuum absorption. It is related in this case to classical orbits of the electron that escape within 20–25 cyclotron times.

(3) We identified a regular family of nearly planar quantum states by quantizing three-dimensional tori. We labeled each state with three integer numbers: n is the total action, n_ϕ is the action of the angular motion, and n_z is the action of the z motion.

ACKNOWLEDGMENTS

The authors thank NSF and DFG for financial support. Also, D.M.W. and J.B.D. thank V. Kondratovich for many discussions.

APPENDIX A: THEORY OF THE CHIRPED FOURIER TRANSFORM

Suppose we have a signal $A(\omega)$ that is a superposition of chirped waves and is defined as

$$A(\omega) = \sum_k \exp[iS_k(\omega)] f_k(\omega) C_k . \quad (A1)$$

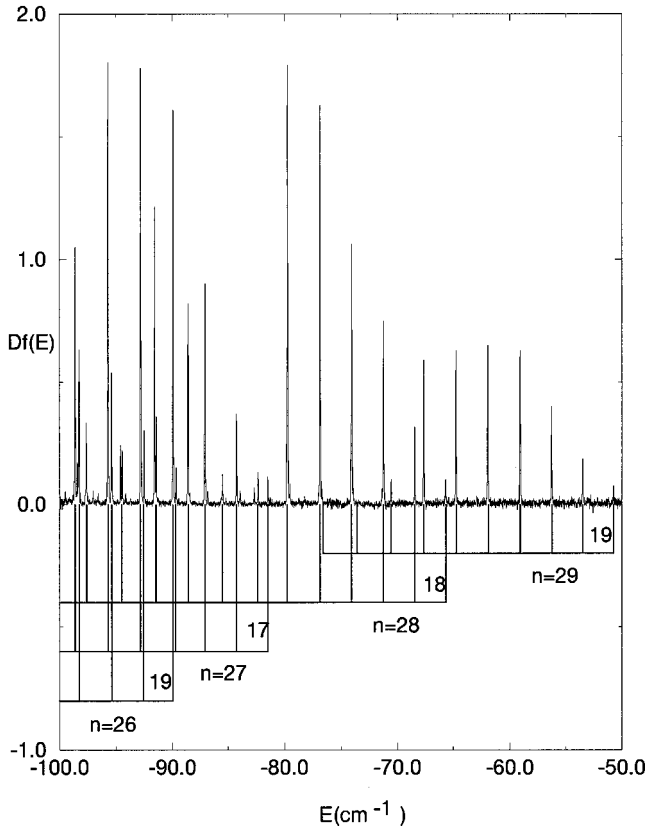

FIG. 13. The measured delayed absorption spectrum at $F=1000$ V/cm and $B=6.002$ T. The quantum states are organized by the principal quantum numbers n and the angular quantum number n_ϕ corresponding to the principal action and the azimuthal action. The states with the same quantum number n belong to a sequence and the states in the sequence are distinguished by the quantum number n_ϕ.

In our case ω corresponds to E, $A(\omega)$ corresponds to the absorption spectrum as a function of energy, $f_k(\omega)C_k$ corresponds to the recurrence amplitude of a classical orbit, and $S_k(\omega)$ corresponds to the action of the classical orbit. We define $T_k(\omega)=\partial S_k(\omega)/\partial\omega$.

For a first example, suppose we know the functions $S_k(\omega)$ and $f_k(\omega)$, but not the constant coefficients C_k. To determine the coefficients C_k, we multiply the signal by some chosen function

$$g(\omega)\exp[-ir(\omega;p)] \tag{A2}$$

where p is a collection of parameters. If $T_k(\omega)$ and $T_j(\omega)$ are ''well separated'' in a sense that will be defined below, we may define the integral

$$R(p)=\int_{\omega_1}^{\omega_2} g(\omega)\exp[-ir(\omega;p)]A(\omega)d\omega, \tag{A3}$$

with appropriate specification of $g(\omega)$ and $r(\omega;p)$. We call $R(p)$ the chirped Fourier transform. Note that our definition of the CFT in Sec. IV is a special case of this definition.

There are several possibilities for defining $g(\omega)$ and $r(\omega;p)$.

1. Definition A

Let the parameter p be a multiplicative constant, $p=a$, and $r(\omega;a)=aS_j(\omega)$, $g(\omega)=[dS_j(\omega)/d\omega]/f_j(\omega)$, and assume $f_j(\omega)\neq 0$ in the observation range. Then

$$R(a)=\sum_k \int_{\omega_1}^{\omega_2} \exp -i[aS_j(\omega)-S_k(\omega)] \times\left[\frac{dS_j(\omega)/d\omega}{f_j(\omega)}\right] f_k(\omega)C_k d\omega.$$

This is similar to the form used by Bonmassar and Schwartz [17]. The term with $k=j$ is

$$R_j(a)=\int_{S_{min}}^{S_{max}} \exp[-i(a-1)S_j(\omega)]C_j dS_j =C_j\exp[-i(a-1)\bar{S}]\frac{2\sin[(a-1)(\Delta S/2)]}{a-1}, \tag{A4}$$

where $\bar{S}=(S_{max}+S_{min})/2$ and $\Delta S=S_{max}-S_{min}$. Therefore

$$|R_j(a)|^2=|C_j|^2(\pi\Delta S)\,\delta_{\Delta S}\left(\frac{a-1}{2}\right), \tag{A5}$$

where $\delta_\eta(u)=\sin^2(\eta u)/(\pi\eta u^2)$ is a widened δ function. Thus the term $k=j$ by itself produces a peak at $a=1$, which is called the ''physically interesting'' peak. The height of the peak is proportional to $(\Delta S)^2$, while its width is proportional to $(\Delta S)^{-1}$.

The terms with $k\neq j$ give

$$R_{k\neq j}=C_k\int \exp -i[aS_j(\omega)-S_k(\omega)]\frac{f_k(\omega)}{f_j(\omega)}\frac{dS_j(\omega)}{d\omega}d\omega.$$

We want these terms to be as small as possible. However, they may give significant contributions in two cases:

Case 1. For some $k=k_0$, there exists a value $a=a_0$ such that $a_0S_j(\omega)-S_{k_0}(\omega)\approx\text{const}\equiv S'_{k_0}$, a constant over the whole range of integration, that is, $S_{k_0}(\omega)\approx a_0S_j(\omega)-S'_{k_0}$ We approximate $C_{k_0}f_{k_0}(\omega)/f_j(\omega)\approx\text{const}\equiv C'_{k_0}$. Then the term with $k=k_0$ is

$$R_{k_0\neq j}=C'_{k_0}e^{-iS'_{k_0}}\int_{S_{min}}^{S_{max}} e^{-i(a-a_0)S_j(\omega)}\frac{dS_j(\omega)}{d\omega}d\omega,$$

$$|R_{k_0\neq j}|^2=|C'_{k_0}|^2\pi\Delta S\,\delta_{\Delta S}\left(\frac{a-a_0}{2}\right).$$

Then we get a ''physically uninteresting'' peak at $a=a_0$. The condition $a_0S_j(\omega)\approx S_{k_0}(\omega)+S'_{k_0}$ implies

$$a_0=T_{k_0}(\omega)/T_j(\omega).$$

We say that the "uninteresting" peak at a_0 and the "interesting" peak at $a=1$ are "well separated" if $|a_0-1|$ is larger than the width of the broadened δ function,

$$|a_0-1|=\left|\frac{T_{k_0}}{T_j}-1\right|\gg\frac{1}{\Delta S}.$$

If this condition holds, the uninteresting peak may be large, but it is distinct from the interesting one.

Case 2. For some $k=k_1$, the integral has a stationary phase point, and can be evaluated by the stationary phase approximation. Typically, there exists a range of a values such that for any $a=a_1$ in this range, there exists a frequency $\omega=\omega_0$ in the domain of integration such that

$$a_1=T_{k_1}(\omega_0)/T_j(\omega_0).$$

Then $R_{k_1\neq j}$ can be rewritten as

$$\begin{aligned}R_{k_1\neq j}&=C_{k_1}\int_{\omega_{min}}^{\omega_{max}}\exp -i[aS_j(\omega)\\&\quad-S_{k_1}(\omega)]\frac{f_{k_1}(\omega)}{f_j(\omega)}T_j(\omega)d\omega\\&\approx C_{k_1}\frac{f_{k_1}(\omega_0)}{f_j(\omega_0)}\exp -i[a_1S_j(\omega_0)\\&\quad-S_{k_1}(\omega_0)]T_j(\omega_0)\int_{\omega_{min}}^{\omega_{max}}\exp\\&\quad-i\left[\frac{a_1T_j(\omega_0)'-T_{k_1}(\omega_0)'}{2}(\omega-\omega_0)^2\right]d\omega\\&\approx C'_{k_1}\exp\, i[a_1S_j(\omega_0)-S_{k_1}(\omega_0)]T_j(\omega_0)\\&\quad\times\frac{2\pi}{|a_1T_j(\omega_0)'-T_{k_1}(\omega_0)'|^{1/2}}\\&\quad\times\exp\left(i\frac{\pi}{4}\mathrm{sgn}(a_1T_j(\omega_0)'-T_{k_1}(\omega_0)')\right),\end{aligned}$$

where $C'_{k_1}=C_{k_1}f_{k_1}(\omega_0)/f_j(\omega_0)$. Then again we get a "physically uninteresting" peak at $a=a_1$. The height of the peak is

$$|R_{k_1}(a=a_1)|^2=\left|C'_{k_1}T_j(\omega_0)\frac{2\pi}{|a_1T_j(\omega_0)'-T_{k_1}(\omega_0)'|^{1/2}}\right|^2.$$

Such peaks might be substantial, but they will typically not be as large as those that occur in case 1. In case 1, the phase of the exponential is essentially constant over the whole range of the integration, while in case 2 there is only an isolated stationary phase point; therefore, case 2 gives peaks having heights independent of the range of integration ΔS.

Again such uninteresting peaks are troublesome only if they occur too near to $a=1$.

We use the word "aliasing" to mean the presence of "false" (i.e., physically uninteresting) peaks in $|R(a)|^2$ overlapping with the interesting peak at $a=1$. This form of the chirped Fourier transform can give significant aliasing. For the systems we consider in this paper, we find that a different definition gives better results.

2. Definition B

Change the origin such that $\omega_a=-\omega_b$, let $g(\omega)=1/f_j(\omega)$, and let p represent the set of three parameters (t,α,β), and $r(\omega,p)=t\omega+\alpha\omega^2+\beta\omega^3$. Then

$$\begin{aligned}R(t;\alpha,\beta)=\sum_k\int_{\omega_a}^{\omega_b}\exp\, i[S_k(\omega)-(t\omega+\alpha\omega^2\\+\beta\omega^3)]g(\omega)f_k(\omega)C_kd\omega.\end{aligned}\tag{A6}$$

Let us examine the term $k=j$ first. We expand $S_j(\omega)$ in a power series

$$S_j(\omega)=S_j^0+T_j\omega+\alpha_j\omega^2+\beta_j\omega^3+q_j(\omega),$$

where $q_j(\omega)$ is equal to the remainder of the Taylor series, which is the difference between the three-jet (terms up to third order) and the exact $S_j(\omega)$; we presume $q_j(\omega)$ is small. Then the term $k=j$ is

$$\begin{aligned}R_j(t;\alpha_j,\beta_j)&=C_je^{iS_j^0}\int_{\omega_a}^{\omega_b}e^{i(T_j-t)\omega}d\omega\\&=C_je^{iS_j^0}e^{i(T_j-t)\bar{\omega}}\frac{\sin([(T_j-t)/2)]\Delta\omega}{(T_j-t)/2},\\|R_j(t;\alpha_j,\beta_j)|^2&=C_j^2\pi\Delta\omega\delta_{\Delta\omega}((T_j-t)/2),\end{aligned}\tag{A7}$$

where $\bar{\omega}=(\omega_b+\omega_a)/2$ and $\Delta\omega=\omega_b-\omega_a$. As before, we get a widened δ-function, which is centered at $t=T_j$. We call $R(t;\alpha,\beta)$ the (α,β)-chirped time spectrum of the signal.

Next we examine a term with $k\neq j$ to look at aliasing. Any term with $k\neq j$ is

$$\begin{aligned}&R_{k\neq j}(t;\alpha_j,\mathrm{B}_j)\\&\quad=C_ke^{iS_k^0}\int e^{i(T_k-t)\omega+(\alpha_k-\alpha_j)\omega^2+(\beta_j-\beta_k)\omega^3+q_j(\omega)}\\&\quad\times\frac{f_k(\omega)}{f_j(\omega)}d\omega.\end{aligned}$$

Then there is a stationary point when

$$(T_k-t)+2(\alpha_k-\alpha_j)\omega+3(\beta_j-\beta_k)\omega^2=0.$$

For example, when $t=T_k$, there is a stationary phase point at $\omega=0$. Suppose the cubic term is negligible and again $C_kf_k(\omega)/f_j(\omega)\approx\mathrm{const}=C'_k$; then the integral is estimated as

$$|R_{k\neq j}|^2=\left|C'_k\int_{\omega_1}^{\omega_2}e^{i(\alpha_k-\alpha_j)\omega^2}d\omega\right|^2=|C'_k|^2\frac{\pi}{|\alpha_k-\alpha_j|}.$$

The height of the main peak increases in proportion to $(\Delta\omega)^2$, but this peak does not. If α_k and α_j are well separated and $|C_k/C_j|\sim O(1)$, then the "false" peaks are smaller than the "real" peak.

TABLE II. The (α,β,γ) values for the five shortest closed orbits from three different methods.

Orbit	Parameters	Taylor	NLLS	Experiment
1	α (units of 10^{-2})	0.06	0.07	0.07
	β (units of 10^{-6})	17.0	20.0	20.0
	γ (units of 10^{-2})	0.80	0.80	0.80
	T	0.34	0.34	0.34
2	α (units of 10^{-2})	0.12	0.12	0.12
	β (units of 10^{-6})	1.88	1.95	2.00
	T	0.68	0.68	0.68
3	α (units of 10^{-2})	0.22	0.22	0.22
	β (units of 10^{-6})	3.40	3.55	3.33
	T	0.80	0.80	0.80
4	α (units of 10^{-2})	0.30	0.30	0.30
	β (units of 10^{-6})	3.13	3.03	3.20
	T	1.82	1.82	1.82
5	α (units of 10^{-2})	0.17	0.17	0.17
	β (units of 10^{-6})	2.82	2.87	3.33
	T	1.96	1.96	1.96

For the example in Sec. IV and another example in Appendix B, definition B works better than definition A. It is a property of the orbits in our systems that if $T_k \sim a T_j$, then $\alpha_k \sim a\alpha_j$, $\beta_k \sim a\beta_j$; therefore $S_k - aS_j \sim$ const over the observed range. If we use definition A, case 1 frequently occurs and the ''false'' peaks are as large as the physically interesting one; on the other hand, when we use definition B, the undesired integrals have only isolated stationary phase points, and the ''false'' peaks are usually smaller than the physically interesting peak.

All our results in this paper are calculated by definition B. For certain orbits, we include an additional parameter γ, with $g(\omega)=\exp(-\gamma\omega)$. In our calculations, we have tried three methods to determine the parameters (α,β,γ).

(1) Method 1: Experimental method. Suppose we were analyzing experimental data without prior knowledge of the parameters (α,β,γ) of an orbit. Then we would search in the parameter space to maximize the height of a peak at $t=T_j$ in the CFT. We first set β,γ to zero, and gradually adjust α to make the peak at $t=T_j$ as high and narrow as possible. After we reach the optimal α, we then turn on β, and finally turn on γ. That would give an experimental determination of $(\alpha_j,\beta_j,\gamma_j)$.

(2) Method 2: Taylor expansion. Suppose by some means we know the values of T_j, $dT_j/d\omega$, $d^2T_j/d\omega^2$ at some particular ω_0 within the integration range. Then we may set $\alpha=\frac{1}{2}dT_j/d\omega, \beta=\frac{1}{6}d^2T_j/d\omega^2$.

(3) Method 3: Nonlinear least-squares (NLLS) fit. Suppose we have determined theoretically the quantity $S_j(\omega)$ over the whole measured range of ω. Then we can choose (α,β) by a nonlinear least-squares fit over the whole range.

It is obvious that the more *a priori* information we have about $(T_j,\alpha_j,\beta_j,\gamma_j)$, the better the result will be, that is, the physically interesting peaks will be higher and narrower.

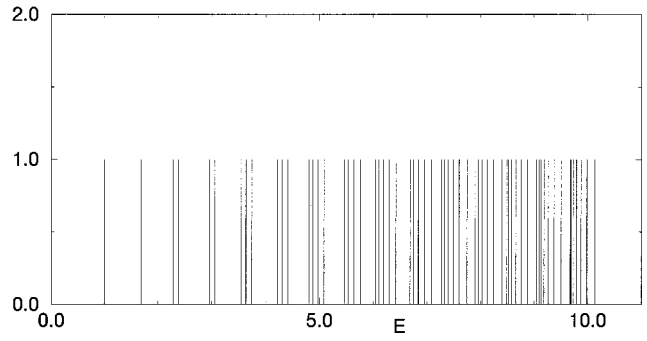

FIG. 14. Energy spectrum of the model Hamiltonian [Eq. (B1)]. Units are not defined for this model. The horizontal axis represents energy, and a line of height 1 is placed at each energy eigenvalue.

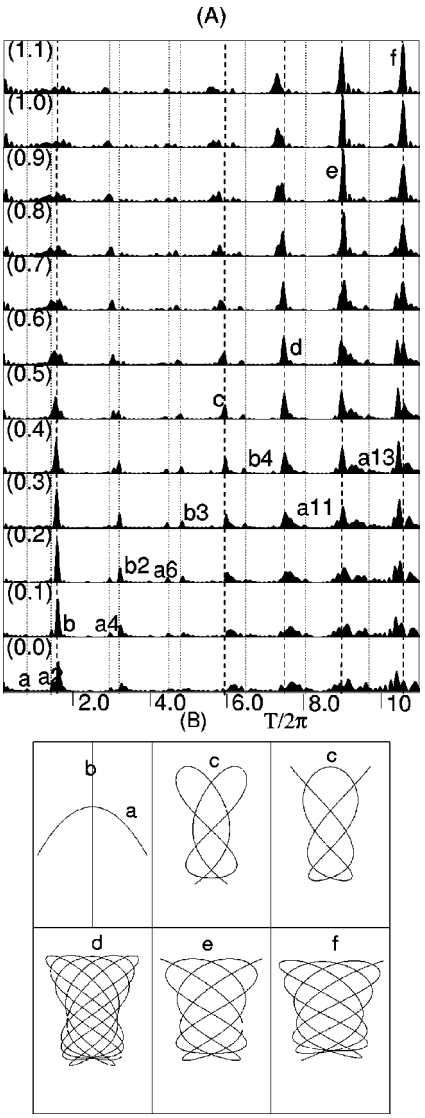

FIG. 15. (a) Chirped Fourier transform of the quantum energy spectrum given in Fig. 14 (units undefined). From the bottom up, we input α values from 0.0 to 1.1 in steps of 0.1. *a, b, c, d, e,* and *f* label peaks that correspond to periodic orbits *a, b, c, d, e,* and *f* shown in (b). $ai(i=2,4,6,11,13)$ labels peaks that correspond to the ith return of the periodic orbit *a*; $bi(i=2,3,4)$ labels the peaks that correspond to the ith return of the periodic orbit *b*.

Also one can go to higher-order terms in a Taylor series, or fit $S_j(\omega)$ to some other functions to get better results. We find that, in our case, a third-degree Taylor expansion is sufficient.

We give values of T,α,β,γ for five of the short orbits in the crossed-field system in Table II. T is the return time of the closed orbits in units of cyclotron times at $E=-95\ \mathrm{cm}^{-1}$. α,β,γ are in units of cyclotron times/cm^{-1}, cyclotron times/cm^{-2}, and cyclotron times/cm^{-1} respectively. These methods all give consistent results.

APPENDIX B: ANOTHER APPLICATION OF THE CHIRPED FOURIER TRANSFORM

As we stated earlier, spectra can be measured by the scaled-variable method for an atom in crossed fields. When it is possible, scaled-variable spectroscopy is a more effective way of extracting recurrences. However, for most systems, scaled-variable spectroscopy is impossible. In this Appendix, we present another application of the CFT to calculate the recurrence spectrum for a model coupled-oscillator system.

The Hamiltonian is similar to that of the Hénon-Heiles system except that it has unequal force constants:

$$H=\frac{1}{2}(p_1^2+p_2^2+\omega_1^2q_1^2+\omega_2^2q_2^2)+\lambda q_2(q_2^2+\eta q_2^2) \quad \text{(B1)}$$

with $\omega_1=1.3$, $\omega_2=0.7$, $\lambda=-0.1$, and $\eta=0.1$.

The quantum energy spectrum, calculated by Noid [28] with a 30×30 (900 functions) harmonic oscillator basis set, is shown in Fig. 14.

The formula for the quantum density of states is

$$\rho(E)=\sum_i \delta(E-E_i).$$

We apply the chirped Fourier transform defined by Eq. (A6) to this density of states:

$$\tilde{\rho}(T;\alpha)=\int e^{-i[T(E-E_0)+\alpha(E-E_0)^2]}\rho(E)dE$$

$$=\sum_i e^{-i[T(E_i-E_0)+\alpha(E_i-E_0)^2]}, \quad \text{(B2)}$$

where α is a parameter.

In this case, the calculation was done with no prior knowledge of the periodic orbits. We evaluated $|\tilde{\rho}(T;\alpha)|^2$ vs T with α ranging from 0 to 1.1 in steps of 0.1. The results are shown in Fig. 15(a). At various values of α, we see sharp, well-resolved peaks. Then orbit calculations showed that these peaks correspond to the periodic orbits drawn in Fig. 15(b).

The peak a at $t/2\pi=0.75$, corresponding to periodic orbit a is weak, but several of its repetitions $a2$, $a4$, $a6$, $a11$, and $a13$ are plainly visible. Orbit b has a period that is slowly varying with energy, so it appears in the ordinary Fourier transform, with $\alpha=0$. However, the peak is sharper when α is set to 0.1, and the successive repetitions of this orbit are visible as peaks $b2$, $b3$, and $b4$, at successively increasing values of α. Orbits $c-f$ are not visible at all in the ordinary Fourier transform, but they show up as large, sharp peaks at appropriate values of α.

Theoretical values of α for peaks $a-f$ are 0.03, 0.07, 0.55, 0.64, 0.87, and 1.02, respectively. These are consistent with the values determined from the CFT graphs within $\pm8\%$.

In cases like this, the scaled-variable-spectroscopy method is impossible. We notice that the CFT extracts strong, narrow, isolated peaks where the ordinary Fourier transform gives no signal. We believe that the CFT is a valuable tool for the study of periodic orbits and recurrences.

[1] Yu. N. Demkov, B. S. Monozon, and V. N. Ostrovskii, Sov. Phys. JETP **30**, 775 (1970); P. A. Braun and E. A. Solov'ev, *ibid.* **59**, 38 (1984); E. A. Solov'ev, *ibid.* **58**, 63 (1983); F. Penent, D. Delande, and J. C. Gay, Phys. Rev. A **37**, 4707 (1988); Robert C. Hilborn, Larry R. Hunter, Kent Johnson, Stephen K. Peck, Alison Spencer, and John Watson, *ibid.* **50**, 2467 (1994); Robert C. Hilborn, Am. J. Phys. **63**, 330 (1995); Jörg Main and Günter Wunner, J. Phys. B **27**, 2835 (1994).

[2] X. M. Tong and Shih-I Chu, Phys. Rev. A **61**, 031401 (2000).

[3] J. Rao, D. Delande, and K. T. Taylor, J. Phys. B **34**, L391 (2001).

[4] G. Raithel and H. Walther, Phys. Rev. A **49**, 1646 (1994); G. Raithel, M. Fauth, and H. Walther, Phys. Rev. A **44**, 1898 (1991).

[5] T. Uzer and David Farrelly, Phys. Rev. A **52**, R2501 (1995).

[6] Charles Jaffé, David Farrelly, and T. Uzer, Phys. Rev. A **60**, 3833 (1999).

[7] Peter M. Koch and David R. Mariani, Phys. Rev. Lett. **46**, 1275 (1981).

[8] Annette Mühlpfordt, U. Even, Eran Rabani, and R. D. Levine, Phys. Rev. A **51**, 3922 (1995).

[9] M. J. Raković and Shih-I Chu, J. Phys. A **30**, 733 (1997).

[10] P. Schmelcher and L. S. Cederbaum [Phys. Rev. A **47**, 2634 (1993)] show some consequences of nuclear motions. If the electron ''escapes'' from the proton, then both electron and proton undergo cyclotron motion and $\mathbf{F}\times\mathbf{B}$ drift. After one proton cyclotron time, they come together again. We believe that this phenomenon is not relevant to the interpretation of the present experiments.

[11] E. L. Stiefel and G. Scheifele, *Linear and Regular Celestial Mechanics* (Springer, Berlin, 1971).

[12] A. Holle, J. Main, G. Wiebusch, H. Rottke, and K. H. Welge, Phys. Rev. Lett. **61**, 161 (1988).

[13] M. L. Du and J. B. Delos, Phys. Rev. A **38**, 1896 (1988); **38**, 1913 (1988).

[14] U. Eichmann, K. Richter, D. Wintgen, W. Sandner, Phys. Rev. Lett. **61**, 2438 (1988); M. Courtney, H. Jiao, N. Spellmeyer, D. Kleppner, J. Gao, and J. B. Delos, Phys. Rev. Lett. **74**, 1538 (1995); J. Main, G. Wiebusch, K. Welge, J. Shaw, and J. B. Delos, Phys. Rev. A **49**, 847 (1994); D. Delande, K. T. Taylor, M. H. Halley, and T. Van der Veldt, J. Phys. B **27**, 2771 (1994).

[15] C. Neumann, R. Ubert, S. Freund, E. Flöthmann, B. Sheehy,

K. H. Welge, M. R. Haggerty, and J. B. Delos, Phys. Rev. Lett. **78**, 4705 (1997).
[16] To our knowledge, this formula has not previously been published, but G. Raithel tells us that he used it to analyze some of the data given in [4]. All notation in this formula is defined in [13].
[17] Alternative definitions of the chirped Fourier transform are given by G. Bonmassar and E. L. Schwartz, IEEE Trans. Pattern Anal. Mach. Intell. **19**, 1080 (1997).
[18] A different method was used by M. Baranger, M. R. Haggerty, and B. Lauritzen, Chaos **5**, 261 (1995).
[19] V. Kondratovich and J. B. Delos, Phys. Rev. A **57**, 4654 (1998).
[20] Eugen Flöthmann and Karl H. Welge, Phys. Rev. A **54**, 1884 (1996).
[21] W. Eastes and R. A. Marcus, J. Chem. Phys. **61**, 4301 (1974).
[22] D. W. Noid and R. A. Marcus, J. Chem. Phys. **62**, 2119 (1975).
[23] D. W. Noid, M. L. Koszykowski, and R. A. Marcus, J. Chem. Phys. **73**, 391 (1980).
[24] Craig C. Martens and Gregory S. Ezra, J. Chem. Phys. **83**, 2990 (1985).
[25] Craig C. Martens and Gregory S. Ezra, J. Chem. Phys. **86**, 279 (1987).
[26] D. M. Wang, Ph.D. thesis, College of William and Mary, Williamsburg, VA, 2000.
[27] Eugen Flöthmann, dissertation, Universität Bielefeld, 1994.
[28] D. Noid, personal communication to J. B. Delos, published in R. T. Swimm and J. B. Delos, J. Chem. Phys. **71**, 1706 (1979).